Sensors and Actuators Reports 6 (2023) 100169

Contents lists available at ScienceDirect

Sensors and Actuators Reports

journal homepage: www.sciencedirect.com/journal/sensors-and-actuators-reports

Design of a microfluidic device for immunoaffinity-based isolation of circulating tumor cells with minimal clogging

Begum Sen-Dogan [a,*], Ender Yildirim [a,b,d], Sebnem Sahin [a], Ebru Ozgur [a], Ozge Zorlu [a], Haluk Kulah [a,c,d]

[a] Mikro Biyosistemler A.S., Ankara 06530, Turkiye
[b] Department of Mechanical Engineering, Middle East Technical University, Ankara 06800, Turkiye
[c] Department of Electrical and Electronics Engineering, Middle East Technical University, Ankara 06800, Turkiye
[d] METU MEMS Research and Application Center, Ankara 06530, Turkiye

ARTICLE INFO

Keywords:
Microfluidic channel
Micropillar
Computational fluid dynamics
Circulating Tumor Cell (CTC) isolation
Immunoaffinity binding

ABSTRACT

Combining bioaffinity-based techniques with microfluidics is an effective strategy for the selective isolation of rare circulating tumor cells (CTCs) among peripheral blood cells. In this scope, designing a microfluidic channel with high cell-surface interaction is crucial, which can be realized by increasing surface area *via* micropillars. In such microfluidic channels, the interpillar distance represents a critical design parameter, and the value is decided considering the trade-off between the possibility of clogging and CTC capture efficiency. In this study, a curvilinear microfluidic channel with a wide (150 μm) interpillar distance was developed to prevent clogging while maintaining high CTC capture efficiency. Computational fluid dynamics was used to compare the residence time of particles in the designed channels. For the proof-of-concept study, microfabricated channels were bio-functionalized for immunoaffinity-based isolation of CTCs, using anti-EpCAM antibodies. Enhanced CTC capture was enabled through the micropillars inside the channels helping the increased encounters between the cells and the antibody-functionalized surface. The curvilinear channel effectively isolated cells from MCF-7 breast cancer cell line among white blood cells, with more than 85% capture efficiency. The rate of non-specific binding of white blood cells remained below 20%. This study demonstrated the ability to increase the interactions between particles and surfaces without requiring a dense layout of the micropillars inside the microchannel, therefore minimizing the clogging possibility of the channel without sacrificing performance.

1. Introduction

Circulating tumor cells (CTCs) present in the peripheral blood are a key cancer biomarker in determining the metastatic potential, disease monitoring, and the effect of the treatment for cancer [1–3]. However, due to the rarity of the CTCs in the bloodstream, especially in the early stages of the disease, it remains a major challenge to detect and isolate these cells from peripheral blood with high specificity and sensitivity. Therefore, the isolation of CTCs requires specialized technologies to overcome the hurdle of finding a couple of CTCs in a background of billions of blood cells.

In the last decade, the utility of microfluidics for the isolation and analysis of CTCs *via* either biochemical or physical isolation processes has been well documented [4–7]. Microfluidics brings the advantage of microscale physics: the surface-area-to-volume (SAV) ratio increases significantly as the fluid dimension decreases from the macroscale to the microscale. A higher SAV ratio creates more opportunities for particles to interact with surfaces within a confined space. Exploiting the advantages of microfluidics, researchers have developed several devices based on various technologies to improve the detection and isolation of CTCs. These include immunoaffinity-based techniques using antibodies targeting cell-surface antigens [7–9], filtration-based size separation [10,11], dielectrophoretic separation [12], inertial sorting [13,14] and acoustophoretic sorting [15]. Among these, immunoaffinity-based techniques stand out as more specific CTC isolation to achieve a higher purity separation. Devices based on immunoaffinity usually consist of an array of pillars in various shapes and arrangements [9, 16–19] to increase the interaction of cells with antibody-functionalized surfaces.

In immunoaffinity-based devices, the adhesive force between a cell

* Corresponding author.
E-mail address: begum.sendogan@mikrobiyo.com.tr (B. Sen-Dogan).

https://doi.org/10.1016/j.snr.2023.100169
Received 19 January 2023; Received in revised form 16 June 2023; Accepted 5 July 2023
Available online 13 July 2023

and a surface consists of the non-specific forces such as van der Waals forces, electrostatic forces, and steric stabilization; and the specific binding of cell-receptors to surface-ligands. Stemming from these different interaction mechanisms, researchers have observed several adhesion types as firm adhesion, transient tethering, and rolling at reduced velocity [20]. When cell capture and adhesive rolling have been studied using microfluidic devices by researchers, it was observed that cells were captured by transient rolling adhesion in the high shear region and by firm adhesion in the low shear region. The adhesive force for rolling cells increased before the cell reached the crest of the cylindric pillars and then decreased afterward [21]. Thus, controlling the shape of the pillar for maximum capture efficiency is essential [22,23].

Aside from the shape of the pillars, the specifications for their arrangement within the channel are also critical. Small interpillar distances (~25 μm), which are comparable to the typical size range of CTCs (12–20 μm in diameter), increase the probability of interaction of CTCs with the surface [7]. However, these narrow gaps can clog when a captured CTC or other impurities block the flow around the pillar. There are different strategies to minimize clogging such as designing extended channel depths [7], choosing wider interpillar distance [9,24] and adjusting the flow rates [25,26]. It is crucial to find an optimum point while adopting these strategies. Extension of channel depths may result in focusing problems during visual observation of the channel under a microscope. When the interpillar distance is too wide, the cells may not have enough encounters with pillars unless the channel design allows for an increased encounter. Also, increased flow rates to abolish clogging between pillars may cause damage to the cells due to higher shear rates and cells may not have enough time near the biofunctionalized surfaces for the binding reaction to occur between the antibodies and antigens in immunoaffinity-based devices.

In this study, we developed an immunoaffinity-based, clog-resistant, microfluidic CTC capture device composed of a curvilinear channel with airfoil-shaped micropillars. We started with a numerical investigation of different channel geometries in terms of the residence time of particles inside the channel and pressure drop. Then, the selected designs were microfabricated and their performances were compared experimentally using cells from MCF-7 breast cancer cell line as a CTC model mixed with WBCs. CTC capture efficiencies and non-specific WBC binding rates were analyzed to determine the interpillar distance that maximizes the capture efficiency and minimizes the risk of clogging in curvilinear channels.

2. Theory and numerical methods

To analyze the effect of channel geometry and interpillar distance on the microfluidic CTC capture, we designed two channel geometries with different interpillar distances. The first geometry was a standard linear channel defined by a rectangular outline. The second geometry was a curvilinear channel formed by combining a rectangular channel and eight half-circles [27]. Half circles were positioned facing each other at an offset defined by the radius of the circle. Curvilinear outline aimed to exploit the mixing effect by manipulating the flow. Both channel designs are illustrated in Fig. 1 with the addition of symmetric bifurcations for homogenous flow distribution at the inlet and outlet of the channel. The airfoil shaped micropillars and their placement is also depicted in Fig. 1.

The channels had micropillars to increase the surface area and to create obstacles for flow manipulation. Micropillar having NACA 0040 airfoil profile was used to form the micropillar layout (Fig. 1 insets). This airfoil geometry was preferred to increase the particle interaction with the pillar surface by facilitating a particle's rolling motion for longer periods [28], thereby increasing the specific binding chance of the cells to the antibodies immobilized on the microchannel surfaces.

Since MCF-7 breast cancer cell lines were the main target to be captured around the pillars during the proof-of-concept studies, their size was used as the basis to define the minimum pillar gaps. MCF-7 cell line cultured in the laboratory had a mean diameter of 14 μm, with a size range of 12–25 μm. Hence, to prevent clogging when the cells with maximum size were captured between the pillars, the minimum gap (δ_1) was chosen as 75 μm. A wider pillar gap equaling approximately the diameter of 10 CTCs (150 μm) was also studied to minimize clogging between pillars due to captured cells or impurities.

Table 1 shows the different designs studied for the numerical investigation of the effect of micropillar distances. All the channels had the same micropillar shape. However, the distance between them changed and the designs were named after their channel geometry, δ_1, and channel length. δ_1 is defined as the shortest distance between the

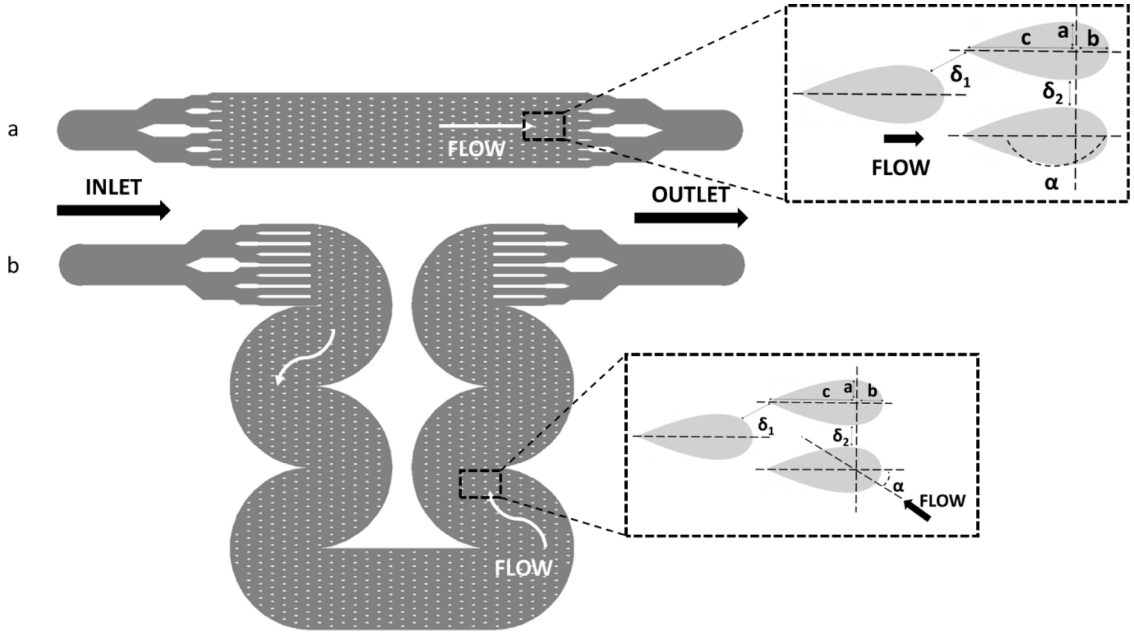

Fig. 1. Designed channel geometries with bifurcations at inlets and outlets. a: linear channel; b: curvilinear channel. Inset schematics show the parameters defining the micropillar layouts where a=20 μm, b=30 μm and c=70 μm for all the micropillars having NACA 0040 profile used in the study. Attack angle (α) is constant at 0° for the conventional linear channel geometry whereas it continuously changes spanning 0°–360° range for the curvilinear channel geometry.

Table 1
Parameters for different channel designs used in numerical studies.

	δ_1	δ_2	α	Channel Length	Channel Volume
LINEAR-150	150 μm	100 μm	180°	7060 μm	0.39 μL
LINEAR-150-LONG	150 μm	100 μm	180°	23,838 μm	1.32 μL
CURVILINEAR-75	75 μm	100 μm	0°–360°	23,838 μm	1.34 μL
CURVILINEAR-100	100 μm	100 μm	0°–360°	23,838 μm	1.37 μL
CURVILINEAR-150	150 μm	100 μm	0°–360°	23,838 μm	1.41 μL

trailing edge of the preceding hydrofoil and the leading edge of the succeeding hydrofoil. Whereas δ_2 is the minimum distance between the curved faces of two neighboring pillars. To study the effect of interpillar distance, δ_1 differed from 75 μm to 150 μm among the designs.

The length of the short linear channel (7060 μm) was chosen based on the shortest possible distance between the inlet and outlet ports of the curvilinear channel. The length of the longer linear channel (23,838 μm) was defined by the average channel length of the curvilinear channel so that it would be possible to compare the effect of the channel geometry for the same length of channels. Micropillars were arranged in the same ordered array where the sharp corner of the airfoil faces the inlet. Although the attack angle inside the linear channels is the same, the curvilinear channel geometry allows the flow to sweep all the attack angles possible.

The designed 2D channels were numerically analyzed using COMSOL Multiphysics 5.2a (COMSOL, MA, USA). The flow was modeled as creeping (Re<<1). The fluid was considered to be an aqueous solution; therefore, the physical properties were assumed to be the same as those of water. Laminar flow with a mass flow rate of 0.05×10^{-6} kg/s (corresponding to ~3 μL/min of volumetric flow rate) was set at the inlet and zero pressure was set at the outlet. At the rigid boundaries, fluid had non-slip boundary conditions. Fig. 2 shows the boundary conditions of the solution domain.

To obtain a grid-independent solution and to minimize inaccuracy originating from discretization, simulations were performed with different mesh sizes (from 470,000 to 1,980,00 mesh elements) using physics-controlled meshing for CURVILINEAR-150 channel design and the pressure drop through the channel versus the number of mesh elements included in the domain was observed. Another data point for a customized mesh with 3,745,000 elements, built using specific controls, was also added to the graph in Fig. 3. Accordingly, it was concluded that the solution converges and becomes independent of the mesh, when the number of elements is greater than 3 million elements as the pressure drop shows less than 0.5% change for around 3 million mesh elements.

The steady-state Navier–Stokes equation (Eq. (1)) and continuity equation for incompressible Stokes flow (Eq. (2)), in the creeping regime, was solved in 2D to determine the velocity field and pressure across the specified domain.

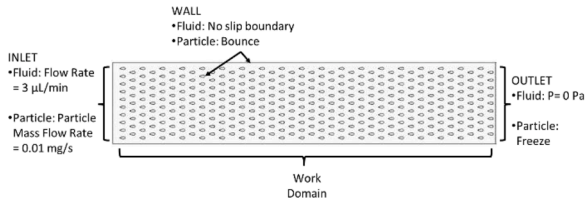

Fig. 2. Simulated linear channel model for 40 μm channel height. Same boundary conditions at inlet, outlet and walls were used for all the channel models. Size of the work domain differed between the channel models.

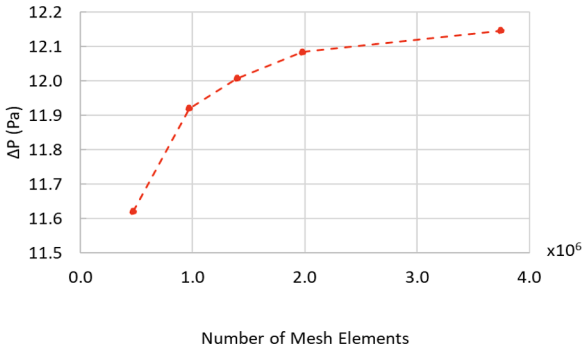

Fig. 3. Convergence of pressure drop along the channel for CURVILINEAR-150 channel design with respect to number of mesh elements included in the domain.

$$\mathbf{u}\cdot\nabla\mathbf{u} = -\frac{1}{\rho}\cdot\nabla p + \nu\nabla^2\mathbf{u} \tag{1}$$

$$\nabla\cdot\mathbf{u} = 0 \tag{2}$$

where, $\mathbf{u}$ (m/s) is the velocity, ρ (kg/m^3) is the fluid density, ν (m^2/s) is the fluid kinematic viscosity, t (s) is the time, and p (kg.m/s^2) is the pressure.

After solving the problem for the velocity field, the particle positions were computed by solving second-order equations of motion for the particle position (Eq. (3)) and Newton's second law (Eq. (4)) with the domination of Drag Force (Eq. (5)) to determine the particle behavior in a steady flow for a specified duration. Then, it was possible to extract the residence time of the particles in the flow for each particle.

$$\frac{d\mathbf{q}}{dt} = v \tag{3}$$

$$\frac{d}{dt}(m\mathbf{v}) = \mathbf{F_D} \tag{4}$$

$$\mathbf{F_D} = 3\pi\mu d(\mathbf{u} - \mathbf{v}) \tag{5}$$

where, $\mathbf{q}$ (m) is the particle position, $\mathbf{v}$ (m/s) is the particle velocity, m (kg) is the particle mass, $\mathbf{F_D}$ (N) is the drag force, d is the particle diameter, and μ (Pa.s) is the fluid viscosity.

Particles were released at the inlet boundary at a rate corresponding to one particle for each mesh element. To simplify the model, particles were accepted to bounce from all the boundaries instead of sticking on the surfaces with a probability value.

Modeling the CTC transport in microfluidics at the cellular level is challenging because the nonlinear deformation of the cells influences the flow, and the flow deforms the cells as well [21]. To simplify the model, the cells were modeled as point particles instead of nonlinear elastic particles. Since the study was focused on the channel structure comparison, the point particle model is sufficient to elaborate on the channel structures, and a more complex particle model would not add further insight that would change the findings of the study. Furthermore, the particles were assumed to be solid spheres that bounce from all the boundaries instead of sticking on the surfaces. At the rigid boundaries, fluid had non-slip boundary conditions. Particles were frozen when they reached the outlet, and their statistical value (position and time to reach the frozen position) was collected at the specified domain when they crossed a pass-through boundary. Residence time values for each particle, which is the duration for a particle to reach the outlet after entering the channel, were recorded. Also, pressure drop (ΔP), the difference in total pressure between the inlet and the outlet of the channel, was computed for each channel design for comparison.

3. Materials and experimental methods

3.1. Materials

Glutaraldehyde solution (GA, 25% in H_2O (w/v), G5882), 3-aminopropyl (triethoxysilane) (APTES, 440140) and streptavidin from *Streptomyces avidinii* (StA, 85878) were purchased from Sigma Aldrich, MO, USA. Bovine serum albumin (BSA, 10% w/v in PBS, 37525) was purchased from Thermo Fisher, MA, USA. Phosphate buffered saline solution (PBS, pH 7.4) was purchased from Biological Industries, CT, USA. Biotinylated anti-EpCAM antibody (AbB, VU-1D9, ab79079) was purchased from Abcam, Cambridge, UK.

3.2. Microfabrication

The channels were fabricated at CSEM (Switzerland) using silicon-glass microfabrication. Firstly, the silicon wafers were cleaned with piranha and BHF solutions. The channel designs were transferred onto the wafers by using standard photolithography processes. The channels were then formed by deep reactive ion etching (DRIE) at 40 μm depth from the front-side of the wafer. Then, the through-holes for fluidic connections were formed with further DRIE from the backside of the wafer. After chemical cleaning, a 300 nm thick thermal oxide layer was formed on the channel surfaces. To seal the channels, silicon wafers were bonded with pristine glass wafers by anodic bonding. At the final step, the wafers were diced in chips with a footprint of 15.5 mm x 17 mm, each containing a single channel design. The microfabrication steps are summarized in Fig. 4a and a diced chip is shown in Fig. 4b.

3.3. Cell culture, blood collection and sample preparation

Cultured human breast adenocarcinoma cell line (MCF-7, DSMZ, ACC 115, Germany) was used as a CTC model. MCF-7 cells were cultured in a growth medium containing Dulbecco's Modified Eagle Medium – High Glucose (DMEM-HG, Gibco, Thermo Fisher Scientific, 10569010, MA, USA), 10% Fetal Bovine Serum (FBS, Biological Industries, 04-007-1A, CT, USA), 1% Minimum Essential Medium (MEM) Non-Essential Amino Acids (Gibco, Thermo Fisher Scientific, 11140035, MA, USA) and 1% Penicillin-Streptomycin (Sigma-Aldrich, P4333, Germany) at 37 °C with 5% CO_2. When the cells reached 70–80% confluency, they were detached from the culture flask with trypsin-EDTA (0.25%, Sigma-Aldrich, T4049, Germany) and resuspended in phosphate-buffered saline (PBS). Cell Tracker Red CMTPX Dye (Invitrogen, Thermo Fisher Scientific, C34552, MA, USA) was added into cell suspension (5 μM for 1 $\times$ 10^6 cells/mL), incubated for 25 min at 37 °C in the dark, washed with PBS at 300 x g for 5 min and diluted to an appropriate concentration. The cell concentration of the samples was determined by using an automated cell counter (BioRAD TC20, CA, USA).

Blood samples were collected from healthy donors to isolate lymphocytes. Ethical approval for blood collection was taken from the Ethical Committee of Middle East Technical University, Ankara Turkey, and studies performed were in accordance with the ethical regulations under the ethical committee-approved protocols (Protocol number: 2017-FEN-073). Informed consent was taken from each donor. To isolate the lymphocytes, the density gradient centrifugation method (Ficoll Paque Plus, GE Healthcare, 17-1440-02, USA) was used. Anti-coagulant (EDTA) treated blood (2 mL) was diluted with an equal volume of PBS and mixed. Ficoll Paque Plus (3 mL) was added into the centrifuge tube and the diluted blood sample (4 mL) was carefully layered onto the Ficoll Paque Plus and centrifuged at 400 x g for 35 min, at 18–20 °C, without break. The upper layer (plasma) was removed carefully and the buffy coat containing WBCs was collected using a clean Pasteur pipette, transferred to a clean centrifuge tube and washed twice with PBS (6 ml) containing 2% FBS (120 x g, 10 min, at 18–20 °C). After the washing step, the cell pellet was resuspended in PBS, stained with Cell Tracker Green CMFDA Dye (Invitrogen, Thermo Fisher Scientific, C7025, MA, USA) (5 μM for 1 $\times$ 10^6 cells / mL) and incubated for 25 min at room temperature in the dark. After incubation, cells were washed with PBS and diluted to an appropriate concentration. Fluorescently stained MCF-7 cells and WBCs were mixed in a ratio of 1:10 (10^4 MCF-7 cells and 10^5 WBCs / mL), respectively. Although it does not represent the ratio in patient samples, CTC/WBC ratio was kept high to allow accurate quantitative analysis with low analysis volume for design validation purposes.

3.4. Microfluidic setup

Fig. 5 shows the microfluidic test setup used throughout the experimental studies. The flow was supplied from the inlet reservoir

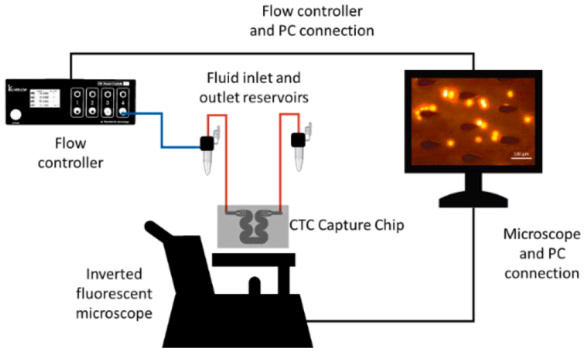

Fig. 5. Microfluidic setup used for all the channel experiments to provide fluid transport and visualization of the channel during the experiments.

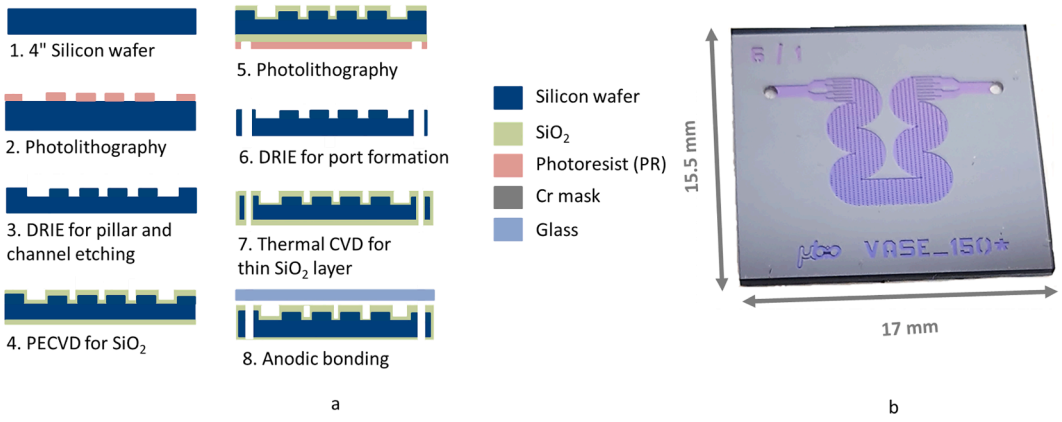

Fig. 4. a: Microfabrication steps for the silicon-glass channels with MEMS technology; b: Front face of the microfabricated silicon-glass chip (CURVILINEAR-150).

connected to Elveflow OB1 pressure controller (Elveflow, Paris, France). The flow was controlled using the Elvesys software supplied with the device connected to a computer. An inverted fluorescent microscope (DMi8, Leica Microsystems, Wetzlar, Germany) connected to a computer was used to inspect the channel during the experiments. The microfluidic chip was placed inside a custom-designed chip holder to provide an interface for microfluidic connections. The holder was placed on top of the motorized microscope stage and the microfluidic parts were connected between the reservoirs and the chip holder interface. The inlet reservoir was replaced manually throughout the experiment according to the designated surface modification and sample processing procedures.

3.5. Biofunctionalization of microfluidic channels

The channel surfaces were functionalized with anti-EpCAM antibodies *via* avidin-biotin interaction chemistry. All the liquids used during the experimental part (except the cell suspension) were filtered with 0.22 μm porosity filters before being fed into the microfluidic channel. After assembling the microfluidic system with a pristine channel, ethanol was fed for the conditioning of the surfaces. Then, APTES (2% in ethanol) was fed into the channel (35 μL/min for 7 min) and incubated for one-hour to silanize channel surfaces. After, the channel was washed with ethanol (35 μL/min for 7 min) and PBS (35 μL/min for 7 min). GA solution (2.5% in PBS) was fed into the channel (35 μL/min for 7 min) and incubated for two hours to react with the free amine groups of APTES and leave a reactive aldehyde group on to the surface to interact with the amine groups of the proteins to be immobilized. Later, StA solution (100 μg/mL in PBS) was fed into the channel (35 μL/min for 7 min) and incubated for one hour. Then, for one hour, StA functionalized surfaces were incubated with biotinylated anti-EpCAM antibody (15 μg/mL in PBS) for the immobilization of antibodies. At the final step, surfaces were coated with BSA solution (1 mg/mL in PBS) to decrease the non-specific binding. The channel was washed thoroughly with relevant buffer solutions between each successive step.

Confirmation of the binding steps for biofunctionalization was performed by contact angle measurement and ellipsometry. First of all, biofunctionalization steps were characterized with respect to their wettability change for each step with a goniometer (Attension Theta, Biolin Scientific, Sweden) at METU Central Laboratory based on sessile drop method at room temperature. The results were reported as the average of five different regions of the biofunctionalized surfaces for each step. Contact angles were 64.8±0.6° for the silicon dioxide surface, 82.2±1.8° for the silanized surface, 62.4±1.2° for the glutaraldehyde coated surface, and 54.4±0.6° for the streptavidin-coated surface. Changes in the contact angle for different steps show the increase in hydrophilicity or hydrophobicity with respect to each molecule type as expected.

The success of the surface biofunctionalization was also validated using spectroscopic ellipsometry (V-VASE J.A Woollam Co. Inc., USA) to measure surface thickness after each step of the biofunctionalization. All measurements were taken at an incidence angle of 74° and with the wavelength range varying between 210 nm and 920 nm. Data was processed *via* WVASE® software (J.A Woollam Co. Inc., USA) and ellipsometry parameters were fitted using the Cauchy Law. The best agreement between the experimental data and theoretical model was obtained by using refractive indices of 1.33, 1.19 and 1.45 for silane, glutaraldehyde, and antibody respectively. For the streptavidin layer, the best fitting was achieved for a refractive index value of 1.77. Measurements were repeated twice, and mean values and standard deviations are calculated accordingly. The increase in thickness after the silanization step was found to be 3.81±0.21 nm which corresponds to about 1.5 silane monolayers. The thickness of the glutaraldehyde was measured as 0.85±0.03 nm. When streptavidin was immobilized on the glutaraldehyde layer, thickness increased by 1.16±0.07 nm. After surface functionalization was completed, antibodies were immobilized onto the surface and the layer thickness was measured as 2.37 ± 0.03 nm. Gradual thickness increase at each step suggests that surfaces were modified with the molecule of interest at each step successfully.

3.6. Performance evaluation of microfluidic channels

The performances of the channels were compared by testing them with EpCAM expressing MCF-7 cells spiked into PBS buffer containing background leukocytes isolated from the blood of healthy volunteers. The cell suspension had an MCF-7 to leukocyte ratio of 1:10. After activation of the channel surface with antibodies, MCF-7 – WBC solutions were fed into the microchannel at a flow rate of 3 μL/min for 3 min under video recording of the channel inlet with Leica Video Module. Then, cells remaining in the tubing were washed with PBS at the same flow rate for 2 min. Afterwards, to eliminate the non-specific binding of leukocytes, the microchannel was thoroughly washed with PBS by gradually increasing the flow rate from mild washing (35 μL/min for 2 min) to harsh washing (65 μL/min for 2 min). Fluorescent images of the channel under TXR, FITC and triple fluorescent filters were taken at each step (before feeding the cell suspension, after washing the cells remaining in the inlet tubing, after mild washing, and after harsh washing) with Leica MultiStep Module. Cell counting from the videos and the images was done with custom-design Image and Video Cell Counter software (Aurvis, Ankara, Turkey). CTC capture efficiency was calculated as the percent of the ratio of CTCs remaining in the channel to CTCs entered into the channel. Non-specific binding capture rate was calculated as the percent of the ratio of WBCs remaining in the channel to WBCs entered into the channel. Experimental results are reported as the mean values from at least three replicates with corresponding standard deviation values. To compare the cell capture efficiency values obtained in different channel designs, two-tailed paired t-test was used. Differences in these values were accepted to be statistically significant when the p value was <0.01.

4. Results and discussion

4.1. Numerical results

For the numerical studies, COMSOL simulations have been carried out for designs given in Table 1 to analyze the flow distribution, particle trajectories and particle residence time, which depends on the average particle velocity within the channel, using a user-defined meshing for each channel. Fig. 6a and b shows the streamlines inside LINEAR-150 channel design. They are not disturbed along the channel length presenting a poor interaction of the particles with the micropillars. However, when the flow distribution inside CURVILINEAR-150 is examined (Fig. 6c and d), it is seen that the streamlines are disturbed due to both the pillars and the channel geometry and the flow is more chaotic than the linear channel.

To identify the flow regime, Reynolds number was calculated theoretically at the narrowest parts of the channels. For the CURVILINEAR-150 channel, maximum Reynolds number was around 0.13 at the 100 μm gap spacing when the maximum velocity was around 2 mm/s. This validates creeping flow regime ($Re<<1$).

For the quantitative comparison of the designs, data obtained for the residence time of particles inside the channels were fitted using the Gaussian model (Fig. S.3), and the mean values of the fitted plots were compared (Fig. 7). Particles spent ~36% more time inside the curvilinear channels than inside the linear channel with the same length and micropillar distance (LINEAR-150-LONG). This was due to the increased interactions between micropillars and particles in the curvilinear channel. These results show that in pillared microchannels, particle residence time, and hence the surface interaction, can be increased significantly by modifying the channel geometry, even if the interpillar distance is much higher than the particle size. In Fig. 7, it is also observed that channel geometry is more in the foreground than

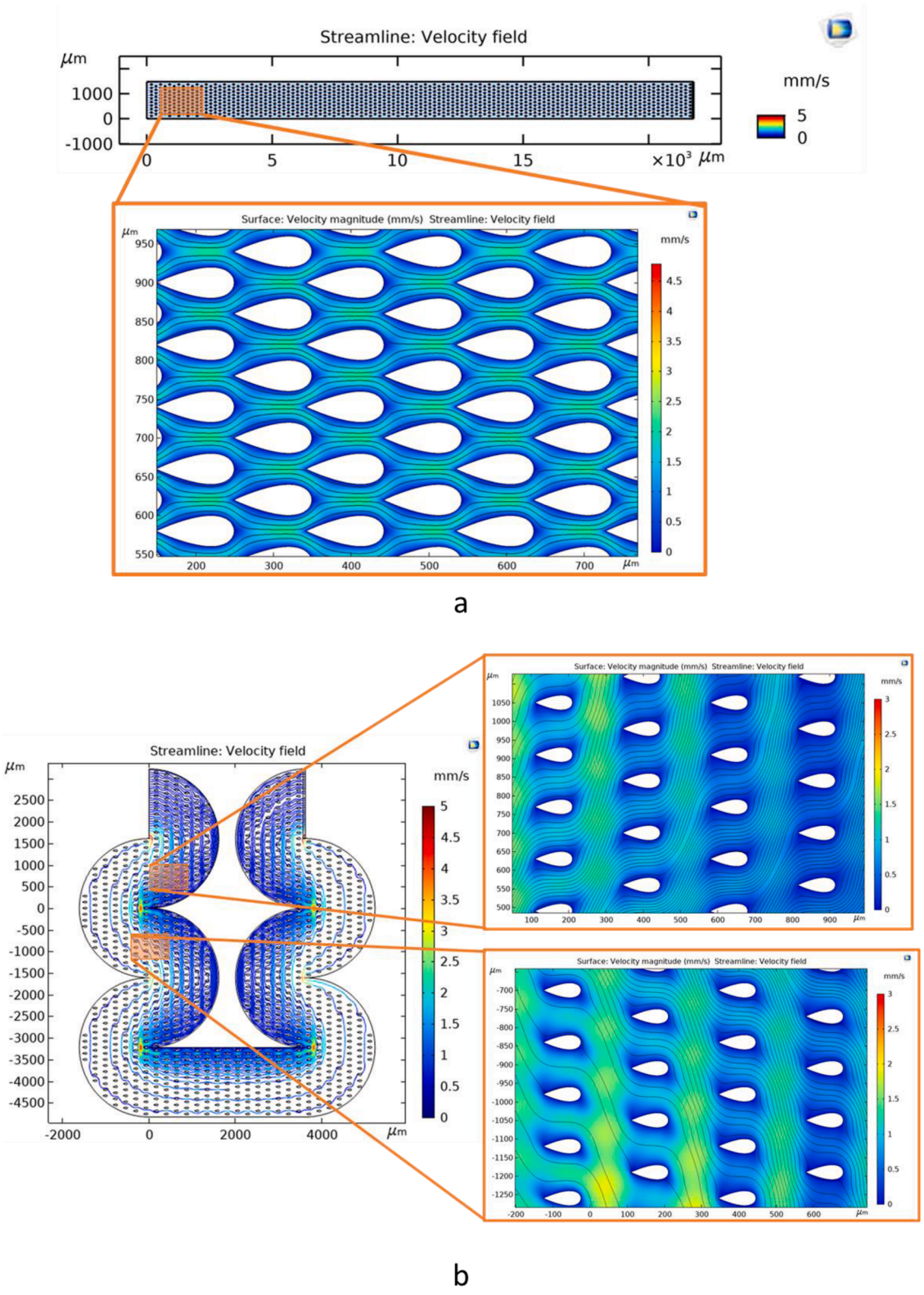

Fig. 6. a: Streamlines inside linear channel LINEAR-150 with close-up view near the inlet; b: Streamlines inside CURVILINEAR-150 channel with close-up views for two different regions at a constant flow rate.

interpillar gaps since the residence time is very similar for curvilinear channels. Furthermore, the same figure shows that pressure drop per length along the channel decreases with increasing pillar gap. This brings the benefit of easier (lower-pressure) operation.

4.2. Experimental results and discussion

For high capture efficiency in immunoaffinity-based rare cell isolation, increasing the possibility of the cells interacting with the antibody-coated microchannel surfaces is critical. To increase the cell-surface

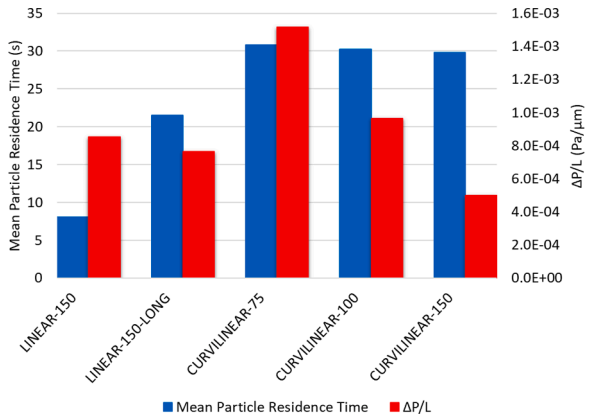

Fig. 7. Comparison of particle residence time and pressure-drop per length inside the modelled linear and curvilinear channels with different interpillar distances under constant flow rate. The pressure drop was calculated between the inlet and outlet of the numerical model which did not include the bifurcations and auxiliary elements such as tubing which were the dominant hydraulic resistance source.

interaction, shorter interpillar distances comparable to the cell size are usually implemented [7]. However, as foreseen, it is observed during experiments with a conventional inter-pillar gap of 25 μm channel design (LINEAR-25: same properties with LINEAR-150 but with δ_1=25 μm) that such designs with narrow gaps are very prone to channel clogging, mostly due to impurities stemming from solutions and auxiliaries used. The initial experiments with LINEAR-25 showed a high occurrence of clogging inside the channel, even during the surface modification step, where all liquids were filtered, due to the airborne impurities or the impurities stemming from microfluidic channel auxiliaries. Different strategies such as filtering liquids, flushing the channel with harsh washing, or using reversed flow stream for surface modification only partially resolved the problem. This showed that channels with narrow gaps might not be very robust in terms of clogging unless a very controlled environment for testing was adopted. Increasing the interpillar gap, on the other hand, adversely affects the capture efficiency due to the decreased cell-surface encounters under flow. To solve this problem, we have designed a microfluidic device with a curvilinear channel geometry to facilitate mixing and cell-surface encounters; and hydrofoil-shaped micropillars with wider interpillar distances to minimize clogging. Several designs with different interpillar distances (75–150 μm) were made to optimize the CTC capture efficiency and minimize clogging. The depth of the channels was chosen as 40 μm to prevent focusing problems during visual observation of the channels under a microscope. Since widening of one dimension in narrow regions, e.g., the pillar gaps in this study, is enough, the shallow channels were not expected to cause clogging. The designs were experimentally analyzed and compared with the base design (linear channels with 150 μm interpillar gaps).

For the experimental testing of the effect of interpillar distance and curvilinear channel geometry on the CTC capture and clogging, LINEAR-150, CURVILINEAR-75, CURVILINEAR-100 and CURVILINEAR-150 designs were microfabricated and tested with MCF-7/WBC mixtures. Besides these, LINEAR-25 was also fabricated for comparison purposes. On the other hand, LINEAR-150-LONG was not fabricated as it showed low residence time and high pressure drop in numerical studies, depicting low capture efficiency and higher-pressure operation.

4.2.1. *Effect of channel geometry*

Fig. 8 shows the CTC capture efficiency and non-specific binding ratio of linear and curvilinear channels with different micropillar gaps. Drastically low CTC capture efficiency was obtained with LINEAR-150 chips when compared to the LINEAR-25 chips due to lower probability of particle-surface interaction. However, most of the captured cells (either specifically or non-specifically) in LINEAR-25 design was actually trapped within the channel due to impurities clogging the channel and impeding the fluid flow (Fig. S.1.). Because of this, non-specific WBC capture rate before washing had a high mean and standard deviation (36% ±11). After harsh washing to get rid of non-specifically captured cells, most of these WBCs were washed off the channel (11% ±3). The effect of washing on non-specific WBC binding rate in LINEAR-150 design was much lower (decreased from 12% to 6%), further

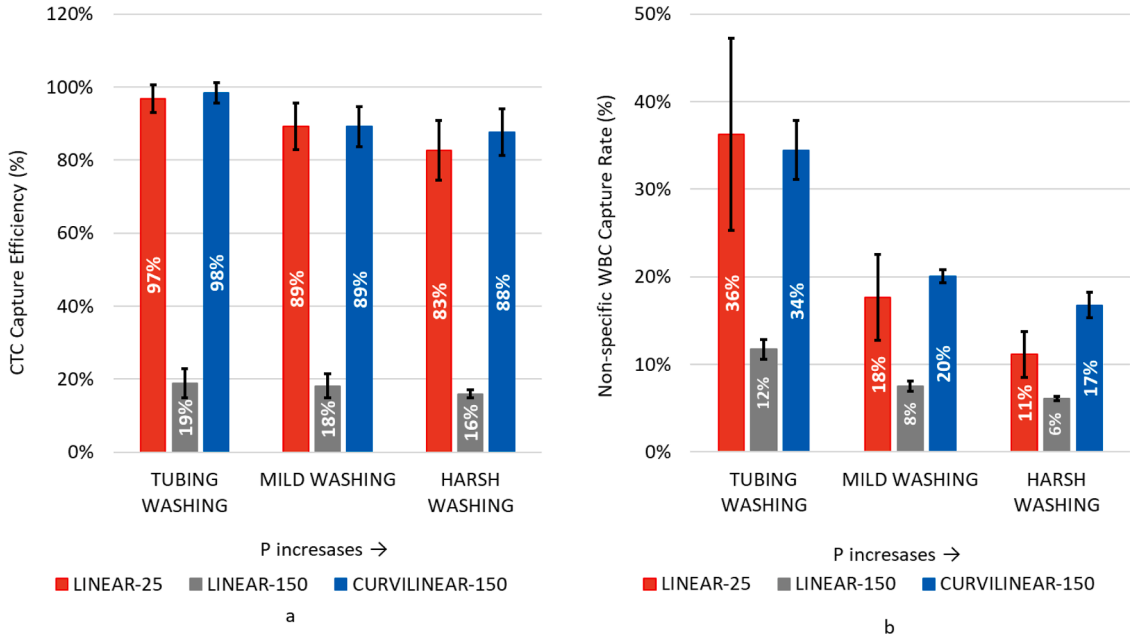

Fig. 8. a: CTC recovery rate for MCF-7 cells and b: non-specific WBC capture rate comparison for linear and curvilinear channels after tubing washing (3 μL/min for 2 min which corresponds to ~90 mbar), mild washing (35 μL/min for 2 min which corresponds to ~1100 mbar) and harsh washing steps (65 μL/min for 2 min which corresponds to ~2000 mbar). Since capillary tubing pieces were used during the study, they are the main source of hydraulic resistance in the microfluidic pathway. The flow sensor was not sensitive enough to measure the small pressure variations (e.g., 1–10 mbar) between the channel types.

showing the effect of clogging on the non-specific capture.

The results (Table S.1) showed that the curvilinear channel with 150 μm gaps (CURVILINEAR-150) has drastically enhanced CTC capture efficiency (by almost 5-fold) compared to the linear channel with the same interpillar gaps (LINEAR-150). The CTC capture efficiency (>80%) is as high as that of the linear channel having 25 μm gaps, without encountering the clogging problem (Fig. 9). Thus, it was demonstrated that providing an increased possibility of cell-surface interaction with the help of a curvilinear channel resulted in more chaotic trajectories and increased capture efficiency and enhanced the robustness of the system without being sensitive to clogging. Although the length of the CURVILINEAR-150 was more than three times of the length of LINEAR-25, its non-specific binding was very similar to that of LINEAR-25, with slightly higher mean values, but significantly lower standard deviation. This is also due to the minimization of clogging issues, leading to more repeatable results and more robust design. One may also argue that the capture efficiency difference between the LINEAR-150 and CURVILINEAR-150 channels are due to the difference in their length. The length of LINEAR-150 is 7060 μm and length of CURVILINEAR-150 23,838 μm (Table 1), which makes the length ratio 3.4 between the two channels. However, since the ratio of their capture efficiency is 5.5 (16% for LINEAR-150 and 88% for CURVILINEAR-150 as stated in Fig. 8) and it is bigger than their length ratio, we can conclude that the length difference is not the only reason between the different performances of the channels. We have observed that the cells adhere mostly in the first one-third part of the linear channels (Fig. S.2), thus, even if the LINEAR-150 were longer, its performance would not increase much. Furthermore, experimental results showing five times increase in capture efficiency with the CURVILINEAR-150 when compared to LINEAR-150 are in well agreement with the numerical simulations depicting almost times higher residence time for CURVILINEAR-150 with respect to LINEAR-150. This shows the validity of our approach of observing the residence time as an indicator of capture efficiency.

4.2.2. *Effect of pillar gaps in curvilinear channels*

To compare the effect of different pillar gaps in curvilinear channels, performances of three channel designs with gaps of 75 μm (CURVILINEAR-75), 100 μm (CURVILINEAR-100) and 150 μm (CURVILINEAR-150) were compared (Fig. 10). Two-tailed paired t-test was performed on these experimental results to check whether the mean difference between them was statistically significant. CTC capture efficiency of CURVILINEAR-150 channel (88%) is similar to efficiencies of CURVILINEAR-100 channel (81%) and CURVILINEAR-75 channel (82%), when the data after harsh washing step are compared ($p<0.01$) (Fig. 10a). Similar non-specific WBC binding rates, ranging from 15% to 20%, were observed after harsh washing step. The results depict that the CTC capture rate efficiency is high even with the large interpillar gaps implemented, while the non-specific WBC capture rate is not affected drastically, based on the interpillar gap within the tested 75–150 μm range. This shows that the cell-surface interaction necessary for specific binding has been successfully established with the curvilinear channel and the non-specific binding has been minimized with the enlarged interpillar gaps. Moreover, the relationship in CTC capture efficiencies obtained experimentally for different pillar gaps were similar to the relationship of residence time values obtained numerically for curvilinear channels. This supports our simplified model for relating the

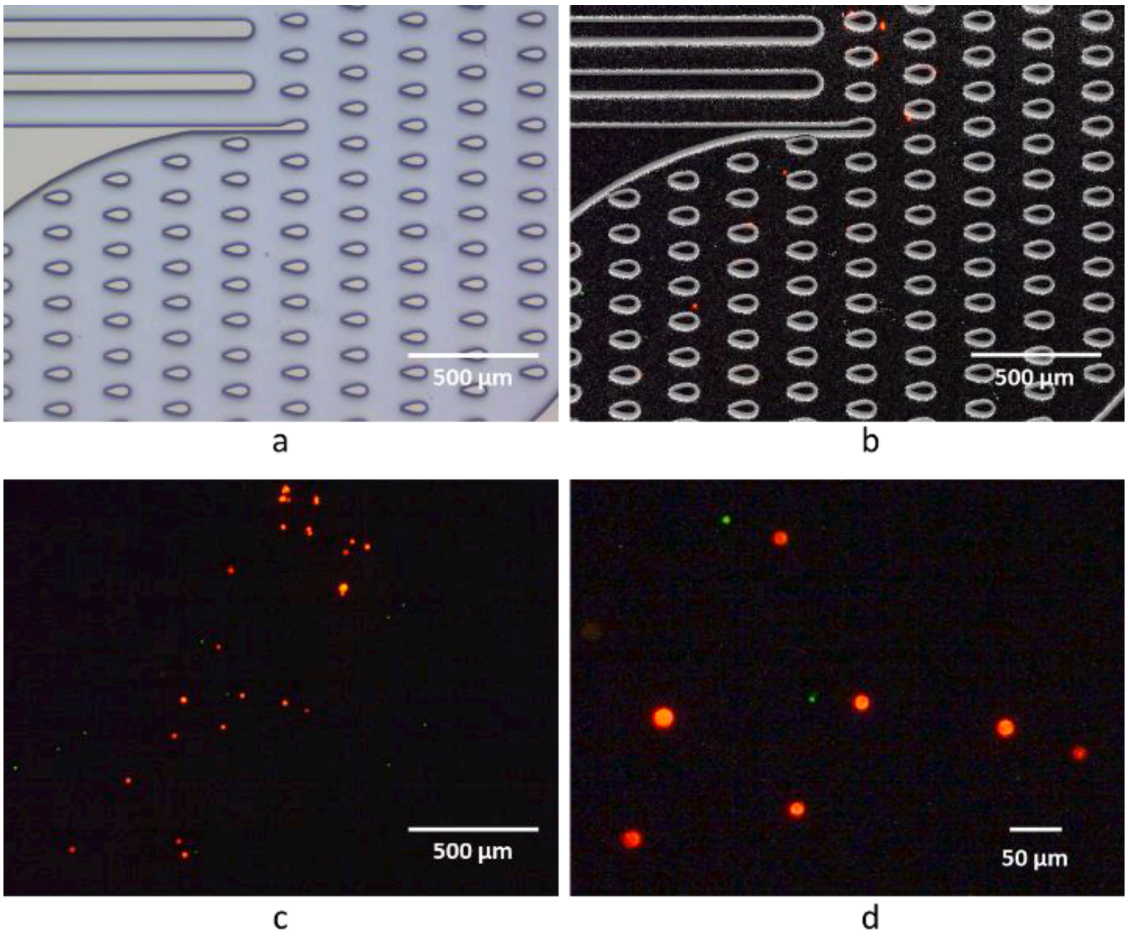

Fig. 9. a: Bright-field image of the CURVILINEAR-150; b, c: captured MCF-7 cells (red) and non-specifically bound WBCs (green) with and without the channel overlay image; d: close-up the captured cells.

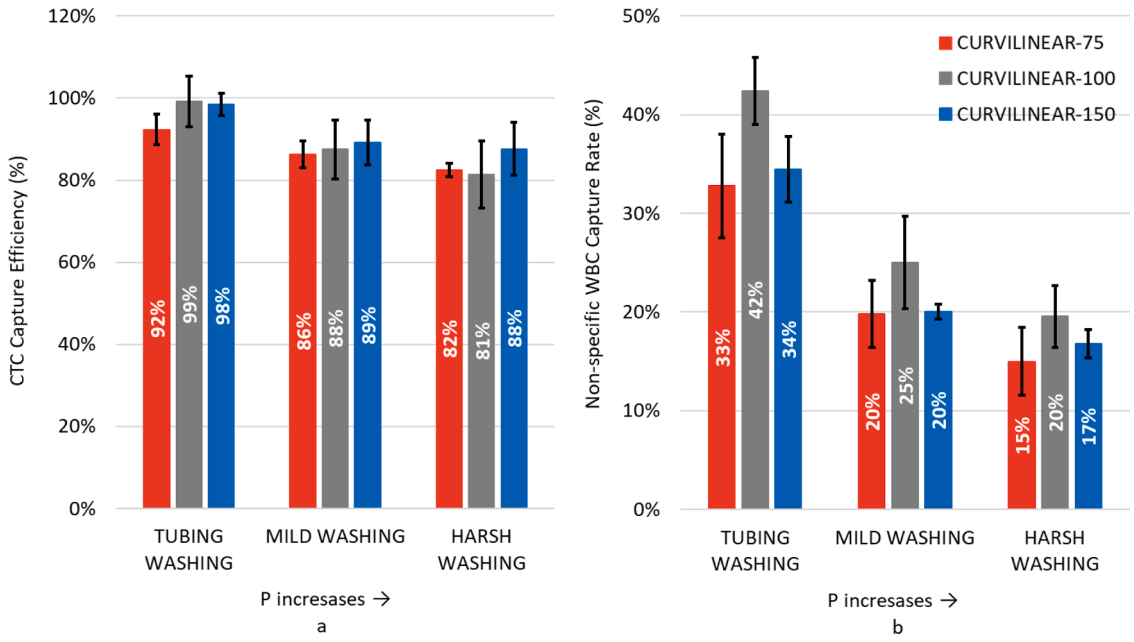

Fig. 10. a: CTC recovery rate for MCF-7 cells and b: non-specific capture rate comparison for curvilinear channels with 75, 100 and 150 μm interpillar distances after tubing washing (3 μL/min for 2 min), mild washing (35 μL/min for 2 min) and harsh washing steps (65 μL/min for 2 min). Experiments were carried out in triplicates and data were given as CTC Capture (%) ± SEM.

residence times and capture efficiencies used during numerical study.

5. Conclusions

Selective isolation of CTCs is crucial for their precise characterization. This paper investigated the effect of interpillar distance inside the microfluidic channels and the effect of channel outer profile on the performance of CTC isolation *via* the immunoaffinity technique with a focus on clogging prevention of the channels. Numerical studies of the different designs were compared in terms of particle residence time inside each channel. Curvilinear channel with wider interpillar gaps showed better performance over the linear channel having similar gaps between the micropillars. The designs were also compared experimentally. MCF-7 cells were captured with immobilized anti-EpCAM antibodies under continuous flow. The curvilinear channels with airfoil-shaped micropillars showed 88% CTC capture efficiency and 17% non-specific binding rate without clogging problems. This performance was similar to the one obtained using a linear channel with narrow gaps however linear channel was often prone to clogging affecting the robustness. Numerical and experimental results were coherent in terms of CTC capture efficiency, although further enhancement in numerical study is possible by implementing particle interactions in the model. However, the aim of this study was to compare the channel geometries using a low-level approximation. Thus, wall effect forces like the Segre–Silberberg effect were not implemented in the model. Furthermore, during the experiments, migration to focusing locations due to the Segre–Silberberg effect was not observed which was consistent with the ideal model created in the numerical study. A similar study [29], Adams *et al.* concluded that they have not observed this effect in the same range of flow regime. Since the scope of this study was the proof-of-concept of the designed channels, the sample volume processed was low as in most of the studies found in the literature. Future work will also include efforts such as parallelization of the channels to increase the sample processing capacity, i.e., the throughput, to adapt the device for the processing of clinical samples collected from cancer patients.

Funding

This research was funded by TÜBİTAK under grant number 7170182.

CRediT authorship contribution statement

Begum Sen-Dogan: Conceptualization, Methodology, Validation, Formal analysis, Investigation, Resources, Data curation, Writing – original draft, Writing – review & editing, Visualization, Supervision, Project administration, Funding acquisition. **Ender Yildirim:** Conceptualization, Methodology, Validation, Formal analysis, Writing – review & editing, Supervision. **Sebnem Sahin:** Investigation, Writing – original draft, Writing – review & editing. **Ebru Ozgur:** Conceptualization, Methodology, Validation, Formal analysis, Resources, Writing – review & editing, Supervision, Project administration. **Ozge Zorlu:** Conceptualization, Methodology, Validation, Formal analysis, Resources, Supervision. **Haluk Kulah:** Writing – review & editing, Supervision, Funding acquisition.

Declaration of Competing Interest

The authors declare the following financial interests/personal relationships which may be considered as potential competing interests: Begum Sen Dogan has patent A MICROFLUIDIC DEVICE FOR SELECTIVE CAPTURE OF BIOLOGICAL ENTITIES issued to MIKRO BIYOSISTEMLER ELEKTRONIK SANAYI VE TICARET A.S. Ender Yildirim has patent A MICROFLUIDIC DEVICE FOR SELECTIVE CAPTURE OF BIOLOGICAL ENTITIES issued to MIKRO BIYOSISTEMLER ELEKTRONIK SANAYI VE TICARET A.S. Ebru Ozgur has patent A MICROFLUIDIC DEVICE FOR SELECTIVE CAPTURE OF BIOLOGICAL ENTITIES issued to MIKRO BIYOSISTEMLER ELEKTRONIK SANAYI VE TICARET A.S. Ozge Zorlu has patent MICROFLUIDIC DEVICE FOR SELECTIVE CAPTURE OF BIOLOGICAL ENTITIES issued to MIKRO BIYOSISTEMLER ELEKTRONIK SANAYI VE TICARET A.S.

Data availability

Data will be made available on request.

Acknowledgments

The authors would like to thank Taylan B. Töral for his support during the microfabrication of the microchannels.

Supplementary materials

Supplementary material associated with this article can be found, in the online version, at doi:10.1016/j.snr.2023.100169.

References

[1] D.F. Hayes, M. Cristofanilli, G.T. Budd, M.J. Ellis, A. Stopeck, M.C. Miller, J. Matera, W. Jeffreyallard, G.V Doyle, L.W.W.M. Terstappen, Tumor cells at each follow-up time point during therapy of metastatic breast cancer patients predict progression-free and overall survival, Clin. Cancer Res. 12 (2006) 4218–4225, https://doi.org/10.1158/1078-0432.CCR-05-2821.

[2] T.M. Deutsch, S. Stefanovic, M. Feisst, C. Fischer, F. Riedel, C. Fremd, C. Domschke, K. Pantel, A.D. Hartkopf, M. Sutterlin, S.Y. Brucker, A. Schneeweiss, M. Wallwiener, Cut-off analysis of ctc change under systemic therapy for defining early therapy response in metastatic breast cancer, Cancers (Basel) 12 (2020) 1–12, https://doi.org/10.3390/cancers12041055.

[3] S. Riethdorf, L. O'Flaherty, C. Hille, K. Pantel, Clinical applications of the CellSearch platform in cancer patients, Adv. Drug Deliv. Rev. 125 (2018) 102–121, https://doi.org/10.1016/j.addr.2018.01.011.

[4] F. Fachin, P. Spuhler, J.M. Martel-Foley, J.F. Edd, T.A. Barber, J. Walsh, M. Karabacak, V. Pai, M. Yu, K. Smith, H. Hwang, J. Yang, S. Shah, R. Yarmush, L. V. Sequist, S.L. Stott, S. Maheswaran, D.A. Haber, R. Kapur, M. Toner, Monolithic chip for high-throughput blood cell depletion to sort rare circulating tumor cells, Sci. Rep. 7 (2017) 1–11, https://doi.org/10.1038/s41598-017-11119-x.

[5] S. Wan, T.H. Kim, K.J. Smith, R. Delaney, G.S. Park, H. Guo, E. Lin, T. Plegue, N. Kuo, J. Steffes, C. Leu, D.M. Simeone, N. Razimulava, N.D. Parikh, S. Nagrath, T. H. Welling, New labyrinth microfluidic device detects circulating tumor cells expressing cancer stem cell marker and circulating tumor microemboli in hepatocellular carcinoma, Sci. Rep. 9 (2019) 18575, https://doi.org/10.1038/s41598-019-54960-y.

[6] C.A. Lemaire, S.Z. Liu, C.L. Wilkerson, V.C. Ramani, N.A. Barzanian, K.W. Huang, J. Che, M.W. Chiu, M. Vuppalapaty, A.M. Dimmick, D. di Carlo, M. L. Kochersperger, S.C. Crouse, S.S. Jeffrey, R.F. Englert, S. Hengstler, C. Renier, E. Sollier-Christen, Fast and label-free isolation of circulating tumor cells from blood: from a research microfluidic platform to an automated fluidic instrument, VTX-1 liquid biopsy system, SLAS Technol. 23 (2018) 16–29, https://doi.org/10.1177/2472630317738698.

[7] M.L. Hupert, J.M. Jackson, H. Wang, M.A. Witek, J. Kamande, M.I. Milowsky, Y. E. Whang, S.A. Soper, Arrays of high-aspect ratio microchannels for high-throughput isolation of circulating tumor cells (CTCs), Microsyst. Technol. 20 (2014) 1815–1825, https://doi.org/10.1007/s00542-013-1941-6.

[8] Y.T. Kang, T. Hadlock, T.W. Lo, E. Purcell, A. Mutukuri, S. Fouladdel, M.D. S. Raguera, H. Fairbairn, V. Murlidhar, A. Durham, S.A. McLean, S. Nagrath, Dual-isolation and profiling of circulating tumor cells and cancer exosomes from blood samples with melanoma using immunoaffinity-based microfluidic interfaces, Adv. Sci. 2001581 (2020) 1–11, https://doi.org/10.1002/advs.202001581.

[9] M. Dickson, P. Tsinberg, Z. Tang, F.Z. Bischoff, T. Wilson, E.F. Leonard, Efficient capture of circulating tumor cells with a novel immunocytochemical microfluidic device, Biomicrofluidics 5 (2011) 1–15, https://doi.org/10.1063/1.3623748.

[10] J. Chudziak, D.J. Burt, S. Mohan, D.G. Rothwell, B. Mesquita, J. Antonello, S. Dalby, M. Ayub, L. Priest, L. Carter, M.G. Krebs, F. Blackhall, C. Dive, G. Brady, Clinical evaluation of a novel microfluidic device for epitope-independent enrichment of circulating tumour cells in patients with small cell lung cancer, Analyst 141 (2016) 669–678, https://doi.org/10.1039/C5AN02156A.

[11] S. de Wit, G. van Dalum, A.T.M. Lenferink, A.G.J. Tibbe, T.J.N. Hiltermann, H.J. M. Groen, C.J.M. van Rijn, L.W.M.M. Terstappen, The detection of EpCAM+ and EpCAM– circulating tumor cells, Sci. Rep. 5 (2015) 12270, https://doi.org/10.1038/srep12270.

[12] V. Gupta, I. Jafferji, M. Garza, V.O. Melnikova, D.K. Hasegawa, R. Pethig, D. W. Davis, ApoStream, a new dielectrophoretic device for antibody independent isolation and recovery of viable cancer cells from blood, Biomicrofluidics 6 (2012) 1–14, https://doi.org/10.1063/1.4731647.

[13] E. Pao, C. Renier, C.A. Lemaire, J. Che, M. Matsumoto, M. Triboulet, S. Srivinas, S. S. Jeffrey, R.P. Kulkarni, M.B. Rettig, E. Sollier, D. Di Carlo, Label-free isolation of prostate circulating tumor cells using microfluidic Vortex technology, Precis. Oncol. (2017) 15, https://doi.org/10.1158/1538-7445.AM2016-4967.

[14] H.W. Hou, M.E. Warkiani, B.L. Khoo, Z.R. Li, R.A. Soo, D.S.W. Tan, W.T. Lim, J. Han, A.A.S. Bhagat, C.T. Lim, Isolation and retrieval of circulating tumor cells using centrifugal forces, Sci. Rep. 3 (2013) 1259, https://doi.org/10.1038/srep01259.

[15] P. Li, Z. Mao, Z. Peng, L. Zhou, Y. Chen, P.H. Huang, C.I. Truica, J.J. Drabick, W. S. El-Deiry, M. Dao, S. Suresh, T.J. Huang, Acoustic separation of circulating tumor cells, Proc. Natl. Acad. Sci. 112 (2015) 4970–4975, https://doi.org/10.1073/pnas.1504484112.

[16] Y.T. Lua, L. Zhao, Q. Shend, M.A. Garcia, D. Wu, S. Hou, M. Song, X. Xu, W. H. OuYang, W.W.L. OuYang, J. Lichterman, Z. Luo, E.M. Posadas, NanoVelcro chip for CTC enumeration in prostate cancer patients, Methods (2013) 64, https://doi.org/10.1016/j.immuni.2010.12.017.Two-stage.

[17] S. Nagrath, L.V Sequist, S. Maheswaran, D.W. Bell, P. Ryan, U.J. Balis, R. G. Tompkins, D.A. Haber, Isolation of rare circulating tumour cells in cancer patients by microchip technology, Nature 450 (2007) 1235–1239, https://doi.org/10.1038/nature06385.Isolation.

[18] B.J. Kirby, M. Jodari, M.S. Loftus, G. Gakhar, E.D. Pratt, C. Chanel-Vos, J. P. Gleghorn, S.M. Santana, H. Liu, J.P. Smith, V.N. Navarro, S.T. Tagawa, N. H. Bander, D.M. Nanus, P. Giannakakou, Functional characterization of circulating tumor cells with a prostate-cancer-specific microfluidic device, PLOS One 7 (2012) 1–10, https://doi.org/10.1371/journal.pone.0035976.

[19] S.L. Stott, C.H.C.H. Hsu, D.I. Tsukrov, M. Yu, D.T. Miyamoto, B. a. Waltman, S. M. Rothenberg, A.M. Shah, M.E. Smas, G.K. Korir, F.P. Floyd, A.J. Gilman, J. B. Lord, D. Winokur, S. Springer, D. Irimia, S. Nagrath, L.V. Sequist, R.J. Lee, K. J. Isselbacher, S. Maheswaran, D. a. Haber, M. Toner, Isolation of circulating tumor cells using a microvortex-generating herringbone-chip, PNAS 107 (2010) 18392–18397, https://doi.org/10.1073/pnas.1012539107, 10.1073/pnas.1012539107/-/DCSupplemental.

[20] X.J. Zheng, L.S.L. Cheung, J.A. Schroeder, L. Jiang, Y. Zohar, A high-performance microsystem for isolating viable circulating tumor cells, Lab Chip 11 (2011) 3269–3276, https://doi.org/10.1109/TRANSDUCERS.2011.5969382.

[21] J. Tan, Z. Ding, M. Hood, W. Li, Simulation of circulating tumor cell transport and adhesion in cell suspensions in microfluidic devices, Biomicrofluidics 13 (2019) 1–15, https://doi.org/10.1063/1.5129787.

[22] L.S.L. Cheung, X. Zheng, L. Wang, R. Guzman, J.A. Schroeder, R.L. Heimark, J. C. Baygents, Y. Zohar, Kinematics of specifically captured circulating tumor cells in bio-functionalized microchannels, J. Microelectromech. Syst. 19 (2010) 752–763, https://doi.org/10.1109/JMEMS.2010.2052021.

[23] S. Mittal, I.Y. Wong, W.M. Deen, M. Toner, Antibody-functionalized fluid-permeable surfaces for rolling cell capture at high flow rates, Biophys. J. 102 (2012) 721–730, https://doi.org/10.1016/j.bpj.2011.12.044.

[24] T. Ohnaga, Y. Shimada, K. Takata, T. Obata, T. Okumura, T. Nagata, H. Kishi, A. Muraguchi, K. Tsukada, Capture of esophageal and breast cancer cells with polymeric microfluidic devices for CTC isolation, Mol. Clin. Oncol. 4 (2016) 599–602, https://doi.org/10.3892/mco.2016.734.

[25] E.J. Mossige, A. Jensen, Separation and concentration without clogging using a high-throughput tunable filter, Phys. Rev. Appl. 9 (2018) 54007, https://doi.org/10.1103/PhysRevApplied.9.054007.

[26] J. D'Silva, R.H. Austin, J.C. Sturm, Inhibition of clot formation in deterministic lateral displacement arrays for processing large volumes of blood for rare cell capture, Lab Chip 15 (2015) 2240–2247, https://doi.org/10.1109/EMBC.2016.7590696.Upper.

[27] B. Şen Doğan, E. Yıldırım, Ö. Zorlu, E. Özgür, A microfluidic device for selective capture of biological entities, (Australian patent no. AU2019416853B2) IP Australia, 2018. https://worldwide.espacenet.com/patent/search/family/071129267/publication/AU2019416853B2?q=pn%3DAU2019416853B2.

[28] C. Luthur Siu-Lun, Z. Xiangjun, W. Lian, C.B. James, G. Roberto, A.S. Joyce, L. H. Ronald, Z. Yitshak, Adhesion dynamics of circulating tumor cells under shear flow in a bio-functionalized microchannel, J. Micromech. Microeng. 21 (2011) 54033, https://doi.org/10.1088/0960-1317/21/5/054033.

[29] A.A. Adams, P.I. Okagbare, J. Feng, M.L. Hupert, D. Patterson, J. Götten, R. L. McCarley, D. Nikitopoulos, M.C. Murphy, S.A. Soper, Highly efficient circulating tumor cell isolation from whole blood and label-free enumeration using polymer-based microfluidics with an integrated conductivity sensor, J. Am. Chem. Soc. 130 (2008) 8633–8641, https://doi.org/10.1021/ja8015022.